



Numerical modeling and experimental validation of thermal history and microstructure for additive manufacturing of an Inconel 718 product

Patcharapit Promoppatum¹ · Shi-Chune Yao¹ · P. Chris Pistorius² · Anthony D. Rollett² · Peter J. Couetts³ · Frederick Lia³ · Richard Martukanitz³

Received: 16 October 2017 / Accepted: 11 January 2018 / Published online: 23 January 2018
© Springer International Publishing AG, part of Springer Nature 2018

Abstract

A product-scale part was additively manufactured from Inconel 718 by laser powder-bed fusion. The thermal and microstructural behavior was experimentally examined to reveal physical characteristics while a high fidelity numerical model was developed to predict characteristics throughout the part volume. Three physical characteristics were considered in the present study: (1) thermal evolution during the build, (2) melt pool configuration, and (3) the final microstructure as-deposited. Thermal simulations were performed by finite element calculation while the microstructure was predicted from the calculated thermal history and existing theoretical correlations. Predicted results were thoroughly confirmed through comparison with experimental measurements. Ultimately, the present work aims to illustrate the integration of the computational method as tools to provide manufacturing qualification for part production by AM.

Keywords Additive manufacturing · Selective laser melting · Finite element modeling · Large-scale modeling · Microstructure · Inconel 718

1 Introduction

Additive manufacturing (AM) has been perceived as revolutionary in the manufacturing industry [1]. The laser powder-bed fusion AM process uses a laser to successively fuse hundreds to thousands of powder layers to form a three-dimensional object. Many notable firms such as General Electric, Siemens, and Aerojet Rocketdyne have incorporated the AM technology to enhance their production capability, investing more than several hundred million dollars [2]. Several alloys including stainless steel, aluminum, and nickel-based alloys are available for powder-bed AM

[3]. Inconel 718 is a precipitation hardenable nickel–chromium alloy known for its high yield strength, weldability, and creep-rupture properties [4], and is the primary focus of the present study. Despite the rapid growth in the AM industry, one of the problems that hinders wider adoption of this technology is the quality of final products [1]. AM production involves various processing parameters, which can dictate product characteristics such as density, microstructure, mechanical properties, residual stress, and distortion. In current practice, multiple process iterations are typically required until acceptable products can be achieved. To reduce the dependence on heuristic iteration, numerical models have emerged as tools to provide insight and improve fundamental understanding of laser–material interactions.

Modeling AM is a multi-scale problem as characteristic times range from milliseconds during the melting of each track to several hours which are typically required to complete part production, and length scales vary from microscopic to macroscopic. Yan et al. developed a powder-scale model to study balling defects for a single scanning track, where simulation results revealed the influence of the surface tension on defect initiation [5]. A similar study on powder-scale effects was carried out by Xia et al. to investigate

✉ Shi-Chune Yao
scyao@cmu.edu

¹ Department of Mechanical Engineering, Carnegie Mellon University, Pittsburgh, PA, USA

² Department of Materials Science and Engineering, Carnegie Mellon University, Pittsburgh, PA, USA

³ Center for Innovative Materials Processing through Direct Digital Deposition (CIMP-3D), Applied Research Laboratory, Pennsylvania State University, State College, PA, USA

the effect of hatch spacing on surface quality [6]. However, while the powder-scale models provide detail of fused track formation and particle-to-particle interaction, they are computationally very expensive and not suitable for layer- and product-scale study. Therefore, many studies considered the powder volume as a continuum to reduce the computational load [7–10]. Thermal behavior during melting and solidification is of great interest as the temperature history could subsequently be used as input for microstructural predictions. Consequently, various studies estimated transient temperatures in the AM process. Thermal measurement in AM machines for model validation is not generally available; the melt pool size has been used in previous studies to indirectly validate thermal models [7, 8, 11]. Promopattum et al. showed predictions of thermal history and melt pool size, and also introduced a numerically-based processing window indicating defect generation mechanisms such as incomplete melting, over-melting, and balling effect [8]. Masoomi et al. numerically investigated the effect of scanning pattern on the thermal history [10]. The calculation was performed for two layers, which revealed that the predicted peak temperature in a melt pool was nearly independent of the scanning pattern, whereas cooling rate and temperature gradient do depend on scanning lengths.

A direct comparison between measured temperatures and simulations has been reported in few studies. Peyre et al. constructed a thin wall consisting of 20 layers, where three thermocouples were placed at the substrate [12]. The thermal prediction was validated by temperature measurements, showing the influence of heat accumulation (from successive layers) on melt pool dimensions. Denlinger et al. used a numerical model to estimate the thermal history of a bulk geometry containing 38 layers, for comparison with in situ temperature measurement during Inconel 718 powder bed fusion [9]. The predicted temperature showed good agreement with the measurements.

Based on thermal models, temperature gradients (G), liquid–solid interface velocities (R), peak temperatures (T_p), and cooling rates (GR) can be predicted; these parameters affect the solidification structure, crystallographic texture, and final microstructure [13]. Previous studies attempted to couple the AM thermal history with existing material correlations to determine the as-deposited microstructure and evolution of solid phases. Sames et al. utilized an analytical solution to calculate the thermal history in electron beam melting of Inconel 718, using a CCT diagram and solidification map to predict microstructure evolution [13]. Results indicated that γ' and γ'' would only appear for extended holding at high temperature, and that the cooling rate to room temperature (after the extended hold at high temperature) has a direct impact on mechanical properties. However, microsegregation can be expected to have a strong effect on phase precipitation, leading to the formation of δ phase

during stress relief [14]. Columnar grains generally form during solidification for AM of Inconel 718 [13, 15, 16]; Liu and To [17] combined the Rosenthal equation and the Hunt columnar-to-equiaxed transition (CET) model [18] for predicting the texture of the epitaxial columnar grains in AM. The primary dendrite arm spacing (PDAS) or cellular spacing is another parameter of interest as it affects mechanical properties [19]. PDAS has been predicted with phase-field modeling [19] and analytical modeling [20, 21]. Liang et al. compared various theoretical PDAS models with experimental results for the laser powder-bed fusion of nickel-based alloys [22]; the analytical model of Kurz and Fisher [23] (KF model) was found to be suitable for PDAS estimation.

Previous studies have utilized numerical models to gain better fundamental understanding of thermal and microstructural behavior in the AM process of Inconel 718. However, most of the models are limited to a single melt pool or, at most, several layers. A numerical model that thoroughly describes the product-scale sample, and that is experimentally validated, is still needed. Such a product-scale model would enable virtual experimentation on AM processes, with opportunities to optimize processing parameters, ensure material properties, minimize the risk of production failure, and accelerate product development [24].

The present study entailed the construction of a sample with a relatively complex geometry and overall dimensions of $16.5 \times 6 \times 7$ cm. The experimental investigation included tracking transient temperatures during the build, sectioning the sample to investigate melt pool configuration, as well as examining and determining the as-deposited microstructure and solidification morphology. For comparison, a finite element model was used for numerical examination of the part. The numerical simulation was performed at Carnegie Mellon University without access to the measurements; sample fabrication and physical measurements were independently performed by CIMP-3D at Pennsylvania State University.

2 Material and experiment

2.1 Inconel 718 powder and the powder-bed fusion AM system

The Inconel 718 powder used in the present study was supplied by EOS. The powder distribution and morphology are shown in Fig. 1a, b. The average powder size was $32.2 \mu\text{m}$. The sample was produced with an EOS M280 powder-bed fusion system, with settings as shown in Table 1. Prior to part building, the building chamber was evacuated and subsequently back-filled with argon to ensure that the oxygen concentration was less than 1000 ppm. The initial base plate temperature was approximately 25°C .

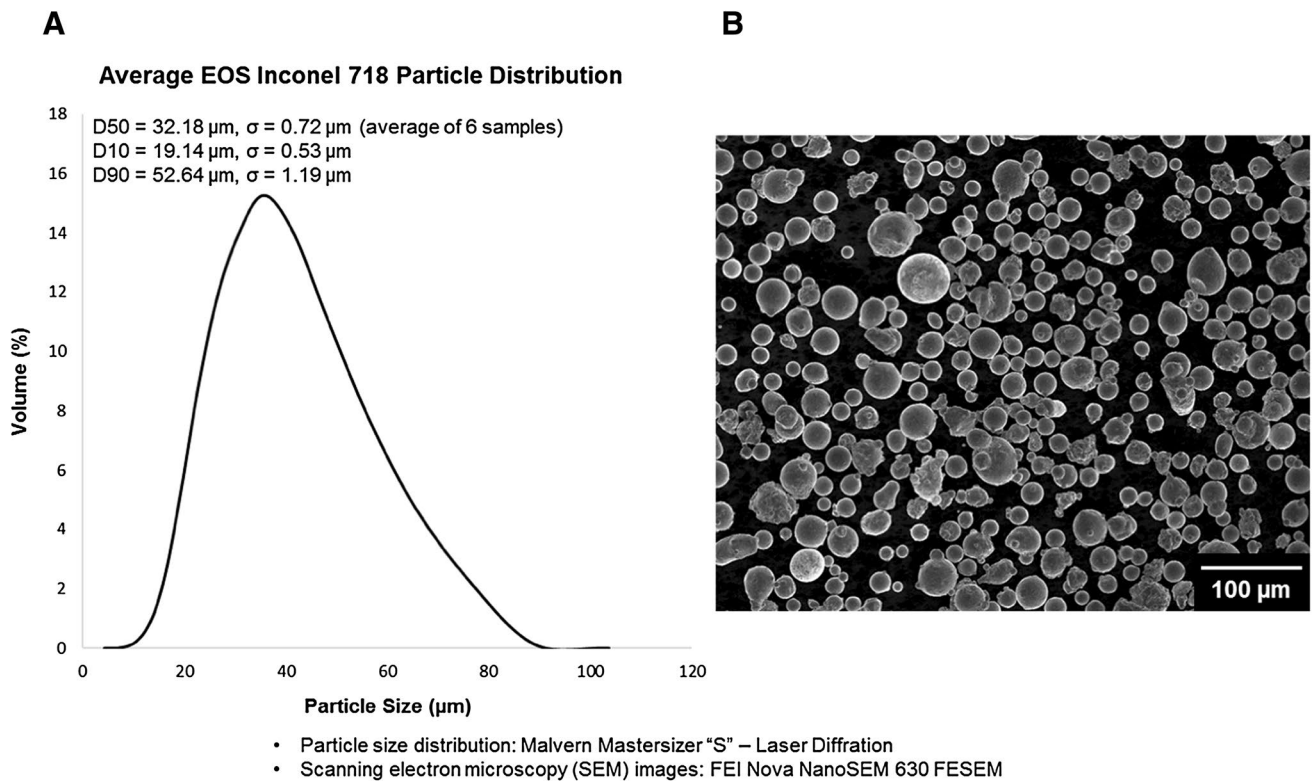


Fig. 1 a Size distribution of EOS IN718 powder and b morphology of powder particles from SEM

Table 1 Processing parameters

Parameters	Values	Parameters	Values
Laser power	285 W	Laser diameter	75 µm
Laser speed	960 mm/s	Laser type	Ytterbium fiber
Hatch spacing	0.11 mm	Wavelength	1070 nm
Scanning stripe width	10 mm	Spot size	70–80 µm
Layer thickness	40 µm	Focal length	410 mm
Recoater material	High speed steel	Time for one layer	40–60 s
		Time between layers	13 s

2.2 Experimental sample

Figure 2a shows the full part geometry. The part geometry was designed to highlight typical thermal, microstructural, and mechanical responses for powder-bed fusion. After part design in CAD software, the part file was transferred to the Materialise Magics software and placed in the center of the build area. The part was designed and placed to align with the laser vector patterns in a predictable fashion. Afterwards, the part file was sliced in EOS RP Tools and then imported into EOS PSW software to generate scanning vectors and assign processing parameters.

The laser hatch direction alternated between parallel and perpendicular to the part geometry in adjacent layers. Odd-numbered layers had hatching parallel to the long axis

of the part; even-numbered layers had hatching perpendicular to the long axis. Within a layer, the hatching pattern was broken into one centimeter wide stripe segments, as shown in Fig. 3. The progression of the stripe during processing was perpendicular to the hatching pattern of that layer and adjacent stripes progressed in opposite directions. Within a stripe, adjacent hatches were also in opposite directions. The sample part contained 1750 layers, with an equivalent build time of approximately 35 h.

A specialized aluminum vault was designed and used during the build to support the substrate and house the temperature data acquisition system. The vault and substrate used during the process are shown in Fig. 2b, c illustrates fabrication of the first layer.

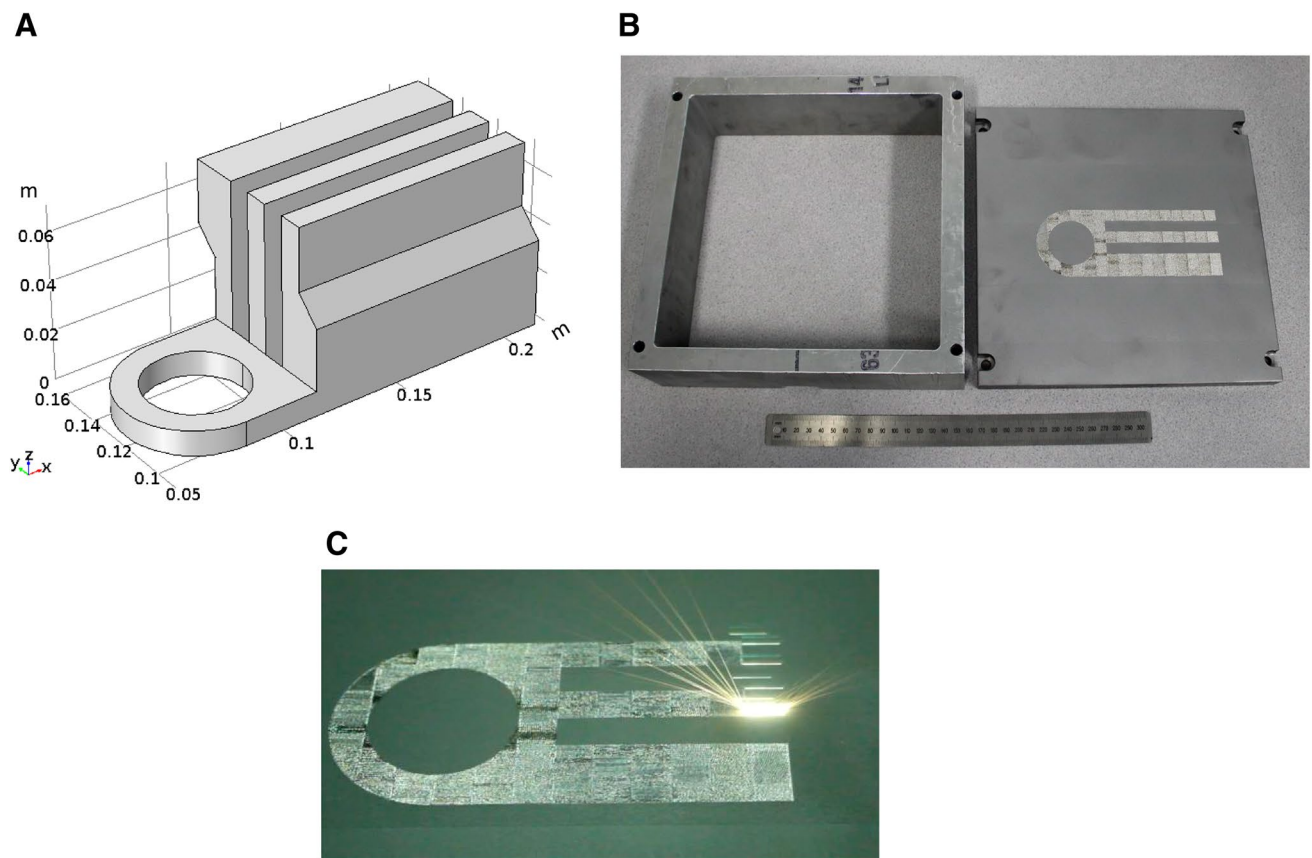


Fig. 2 a Full part geometry, b aluminum stand and substrate, and c fabrication of the first layer

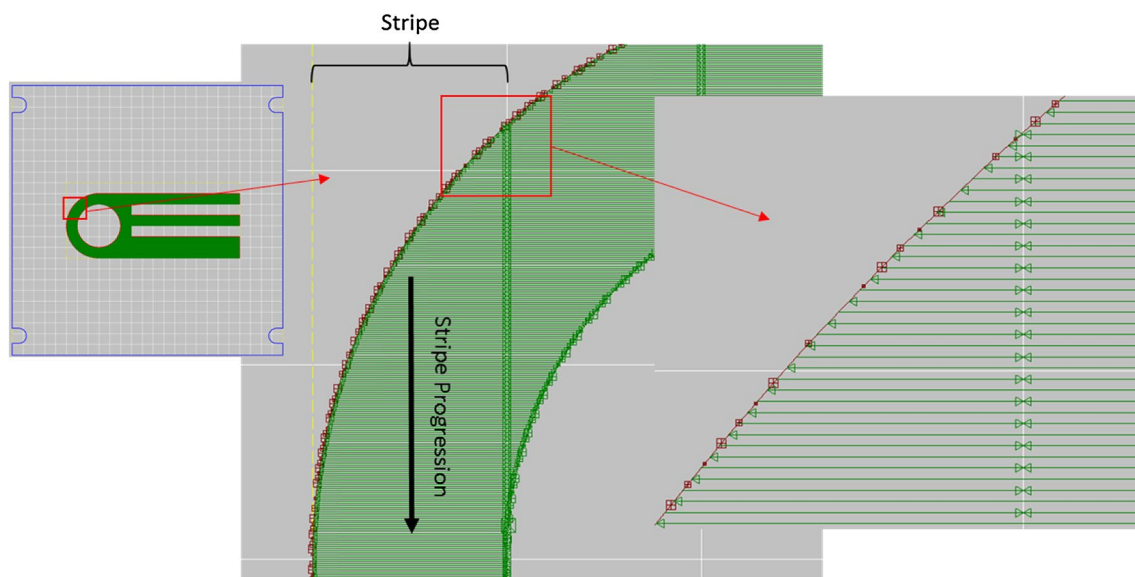


Fig. 3 Laser scanning pattern of one layer at different magnifications

3 Measurement setup and sample preparation

Tungsten–rhenium, C-type thermocouples having a diameter of 270 μm were embedded in the build plate through holes 1.016 mm in diameter that were precision drilled from the bottom of the plate and extended to 0.25 mm below the top surface. Another hole 0.254 mm in diameter was precision drilled from the top surface to accommodate the thermocouple ball. A ceramic tube (1.0 mm diameter) with two internal channels was used to insulate the thermocouple leads. An alumina slurry was used to seal the gap between the thermocouple ball and the ceramic tube. This arrangement enabled the thermocouples to be inserted from the bottom of the plate and the balled end to be seated on the top surface of the plate where deposition of material would occur [25]. A schematic of the arrangement of the embedded thermocouples is shown in Fig. 4. A data acquisition system, National Instruments Model Ni9213 DAQ, and battery pack were utilized within the vault to obtain temperatures at selected locations at the top surface of the substrate during processing. The locations of the thermocouples were selected to represent points of interest on the top surface of the plate, as well as directly below other points of interest. Figure 5 details the exact locations of the embedded thermocouples and the various points of interest within the build sample. During processing, temperatures were recorded at 100 Hz. After completion of the build, the data acquisition system was removed from the vault, and electrical discharge machining (EDM) was used to separate the sample from the build plate, as

well as to remove two vertical slices approximately 6 mm in thickness from the sample at the points of interest.

Specimens from the removed slices that represented the points of interests were prepared for optical microscopy by removing sections using wet cutting with a Struers Labotom-3 and then hot mounted in epoxy resin using a Struers Pronto-Press 2. All samples were ground and polished on a Struers Pedomax-2. Grinding utilized various grits for two minutes, followed by a rinse prior to each subsequent paper. After the samples were ground, the Inconel 718 samples were polished using a 3 micron diamond suspension, a 1 micron diamond suspension, followed by colloidal silica. The samples were electrolytically etched with 10% oxalic acid solution at 1 V for 2 s. Specimens were then examined using optical microscopy.

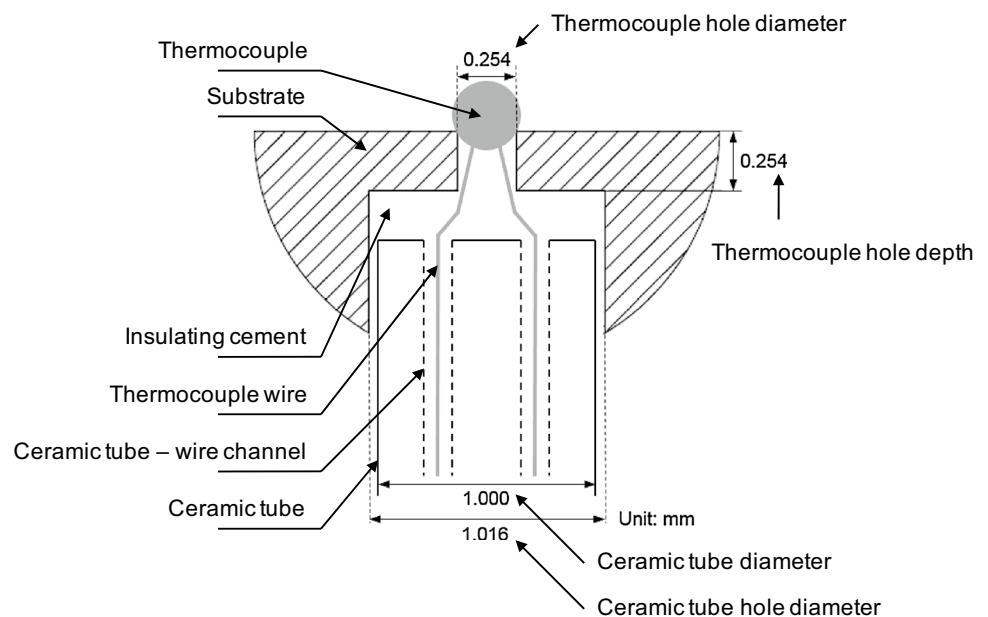
4 Thermal simulation

A three-dimensional FE analysis package, COMSOL, was used to predict the temperature evolution, using temperature-dependent material properties, Gaussian distribution of the moving heat source, heat losses from natural convection and radiation and processing conditions as shown in Table 1.

4.1 Material properties

The thermal conductivity, density, heat capacity, and emissivity as functions of temperatures are shown in Fig. 6, for solid (fully dense and powder), and liquid. An apparent heat capacity method incorporated the latent heat ($L = 210 \text{ kJ/kg}$) during melting and solidification [26]. The melting range,

Fig. 4 Schematic showing details of the embedded thermocouple within the build plate



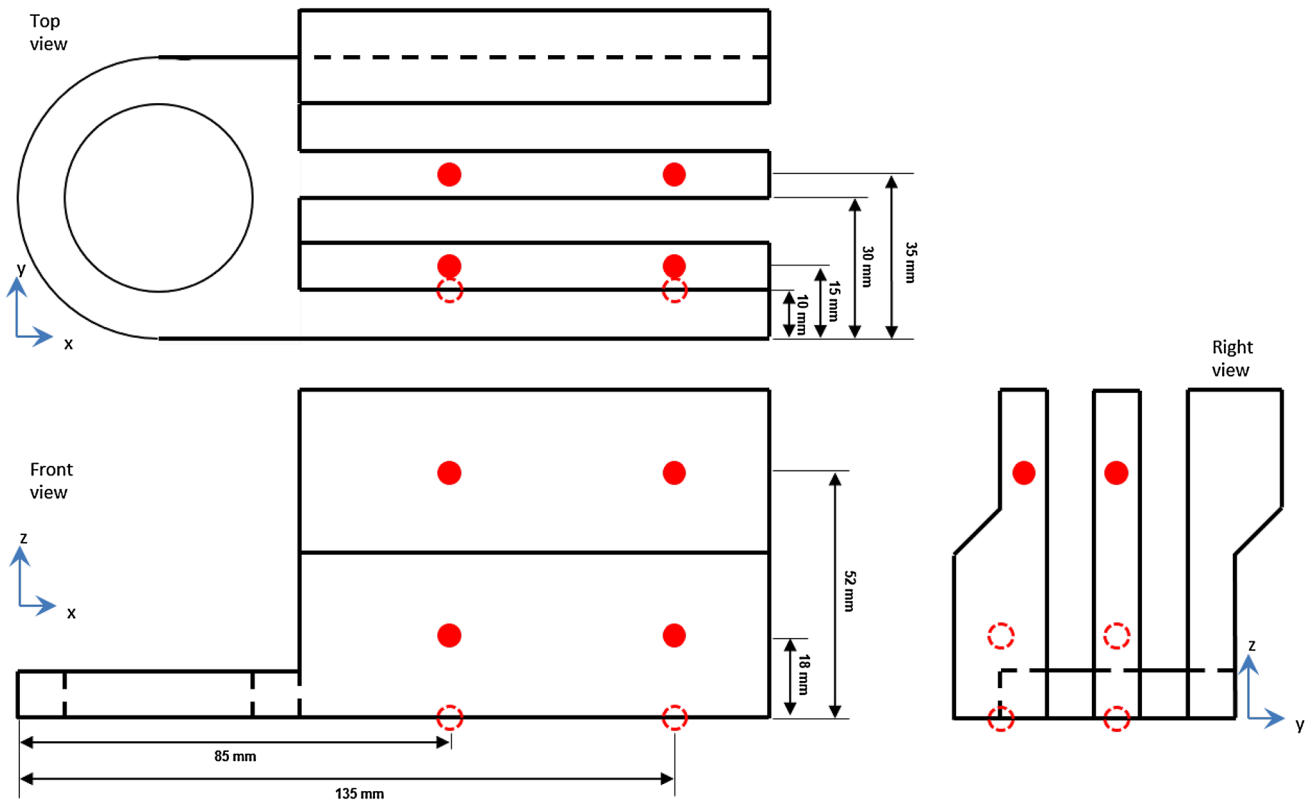
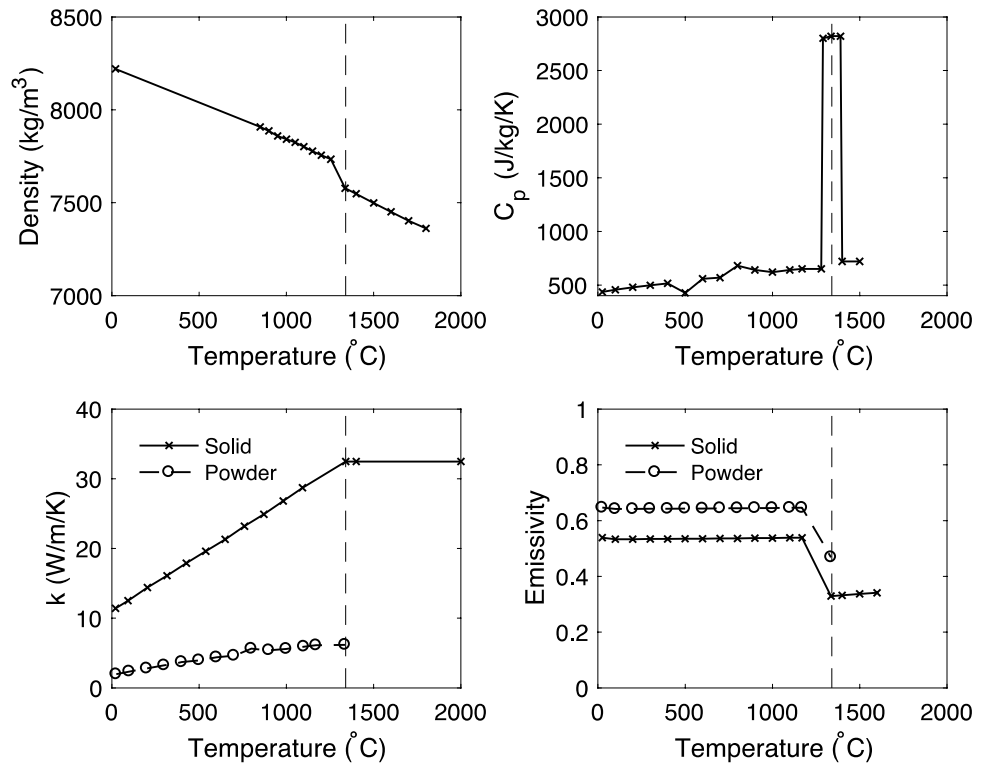


Fig. 5 Schematic of the build showing positions of embedded thermocouples as dashed circles, and points of interest within the sample design

Fig. 6 Thermophysical properties for Inconel 718 as functions of temperature [7]



ΔT_m , is about 200 K, centered on an average melting temperature of approximately 1340 °C [27]; see Eq. (1).

$$C_p = \begin{cases} C_{p,\text{sensible}} & \text{for } T < T_m - 0.5\Delta T_m \\ C_{p,\text{modified}} = C_{p,\text{sensible}} + L/\Delta T & \text{for } T_m - 0.5\Delta T_m < T < T_m + 0.5\Delta T_m \\ C_{p,\text{sensible}} & \text{for } T > +0.5\Delta T_m \end{cases} \quad (1)$$

4.2 Boundary conditions

The thermal model included the substrate and product. The incident laser power was assumed to follow the Gaussian distribution as shown in Eq. (2).

$$q(x, y) = \frac{2\lambda P}{\pi r_0^2} \exp\left(\frac{-2((x - x_0)^2 + (y - y_0)^2)}{r_0^2}\right) \quad (2)$$

where P is the laser power, r_0 is the laser beam radius, and λ is the absorptivity of the material.

The absorptivity for Inconel 718 under a laser with a wavelength of 1.06 μm , which is comparable to the wavelength of the Yb:YAG laser used in the EOS machine, has been reported to vary between 0.3 and 0.87 [7, 28–30].

Radiation from the top surface was quantified using a heat transfer coefficient for radiation:

$$h_{\text{rad}} = \varepsilon\sigma(T^2 + T_0^2)(T + T_0) \quad (3)$$

As boundary conditions, the bottom of the substrate was maintained at room temperature (the measured temperature at this position shows insignificant temperature rise during the production [8]) and the side walls were insulated.

Convection in the melt pool was not considered, which means that the predicted temperatures in the liquid would be too high. However, this simplification has little effect on melt-pool size and temperature transients in the solid.

4.3 Finite element modeling

Thermal simulation of the entire product in AM has been a great challenge due to complex physical phenomena involving various length and time scales. Nevertheless, as the heating process in the AM is highly repetitive, a multiscale modeling technique with simplified heating approach could be used to obtain the complete thermal history in an efficient manner. First, the initial solid temperature from thermal accumulation due to layer addition was determined using planar heating and calculated layer-by-layer up to the height of a plane of interest. Subsequently, calculation of thermal history using a moving laser heat source was carried out to determine the detailed temperature history at the point of interest. In the moving-laser simulation, the heat source moved in a pre-defined geometry, where the material was

first in the powder phase. Once heated and at a material temperature beyond the melting point, the material was per-

manently changed to dense liquid or solid. Thorough examination of simplified scanning strategies with experimental validation can be found in Chiumenti et al. [31].

Mesh sensitivity analysis was performed to ensure that thermal results were independent of the mesh size. Rectangular elements were used with a size between 22 and 342 μm^2 for the moving source calculation, where the small mesh was used in the irradiated area and the mesh size increased with distance away from the heat source. The numerical simulation took 5.5 h for planar heating of the entire product and 40 min for moving-laser heating at each point of interest. The workstation used an Intel Xeon Processor E5 2.8 GHz with 4 cores.

5 Pre-validation of numerical models with existing experimental data

Experimental results from Sadowski et al. [32] were used for initial validation of the numerical model. Sadowski et al. experimentally investigated the width of a single scanning track with various combinations of laser power and scanning speed, where the material and operating conditions were similar to those in the present study. The heat input—Eq. (4)—was used to quantify the effect of laser power and scanning velocity on melt-pool size [33].

$$E = \frac{P}{V} \quad (4)$$

Figure 7a, b display the calculated temperature distribution within and around the melt pool on cross-sectional and longitudinal views. The black solid line shows the liquid–solid interface (melt pool). The simulation was performed with element sizes mentioned in Sect. 4.3. The melt pool configuration was calculated when the size of the liquid pool reached its largest size, which is just before the start of cooling.

Figure 8 compares the average experimentally measured line widths (taken to be the same as melt-pool widths) with predictions from the FE model. To test sensitivity to absorptivity, the numerical estimation was performed for absorptivity values from 0.3 to 0.87; the melt-pool width is expected to be approximately proportional to the square root of the absorptivity [34]. The predictions

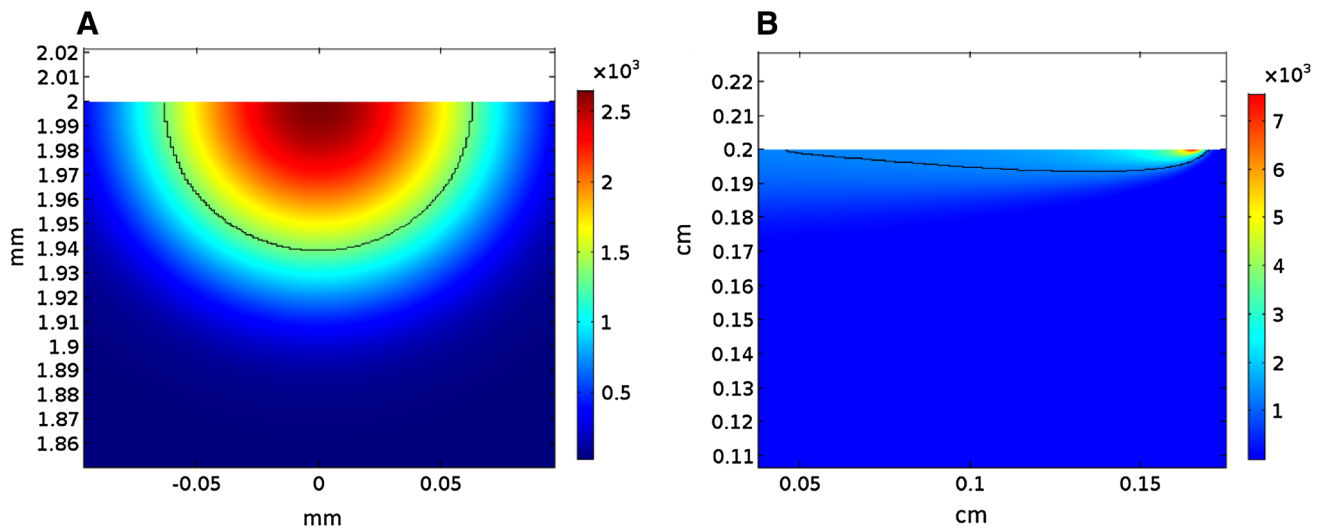


Fig. 7 **a** Cross-sectional view (yz) and **b** longitudinal view (xz) of the calculated melt pool temperature profile ($^{\circ}\text{C}$) and the fusion line (indicated by black line) from the FE calculation (simulated for laser power of 200 W, scanning velocity of 960 mm/s, and absorptivity of 0.5)

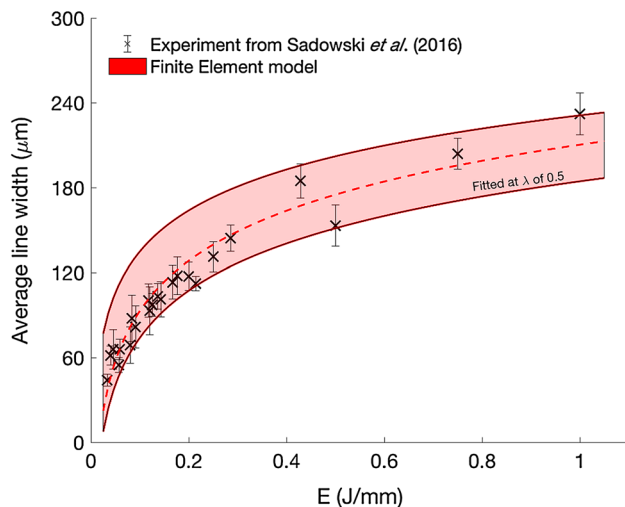


Fig. 8 Comparison of melt pool widths from experiments [32] and predicted with the finite-element model. The shaded area shows the range of predictions with absorptivity from 0.3 to 0.87 while the dashed line refers to the fitted absorptivity

best fitted the experimental values for an absorptivity of 0.5, similar to that previously reported by Montgomery et al. [29].

6 Results and discussion

A thorough comparison between FE simulations and experimental results regarding thermal history and micro-structure is reported here.

6.1 Thermal history comparison

The numerical model provided the thermal history of the complete build. The AM process causes temperature changes on a scale of hours for the complete build and milliseconds for local thermal behavior. Thermal results from the experiment and simulation are presented for both longer and shorter time scales.

6.1.1 Large-scale thermal development

Fig. 9a shows the layer temperature just before deposition of the next powder layer when the temperature on the top surface was relatively uniform. Figure 9a also indicates that higher layers were constructed with locally higher base temperatures due to heat accumulation during the build. The predicted maximum temperature rise from room temperature was approximately 250°C . Figure 9b, c show the predicted temperature history of all 14 points (at the end of layer deposition). The plot illustrates the influence of the overall energy input, geometric features, and fabrication time on the overall temperature increase. For example, Fig. 9b shows a sudden layer temperature drop around 300 min, when building of a thin region at the left-hand side of the geometry was completed, with no further direct heat input above points 1 and 2 (refer to Fig. 10). The sudden layer temperature increase around 500 min was caused by a reduction in scanning time for one layer from 70 to 50 s because of a smaller scanning area. Table 2 summarizes the predicted temperature increase from room temperature when the points of interest were built.

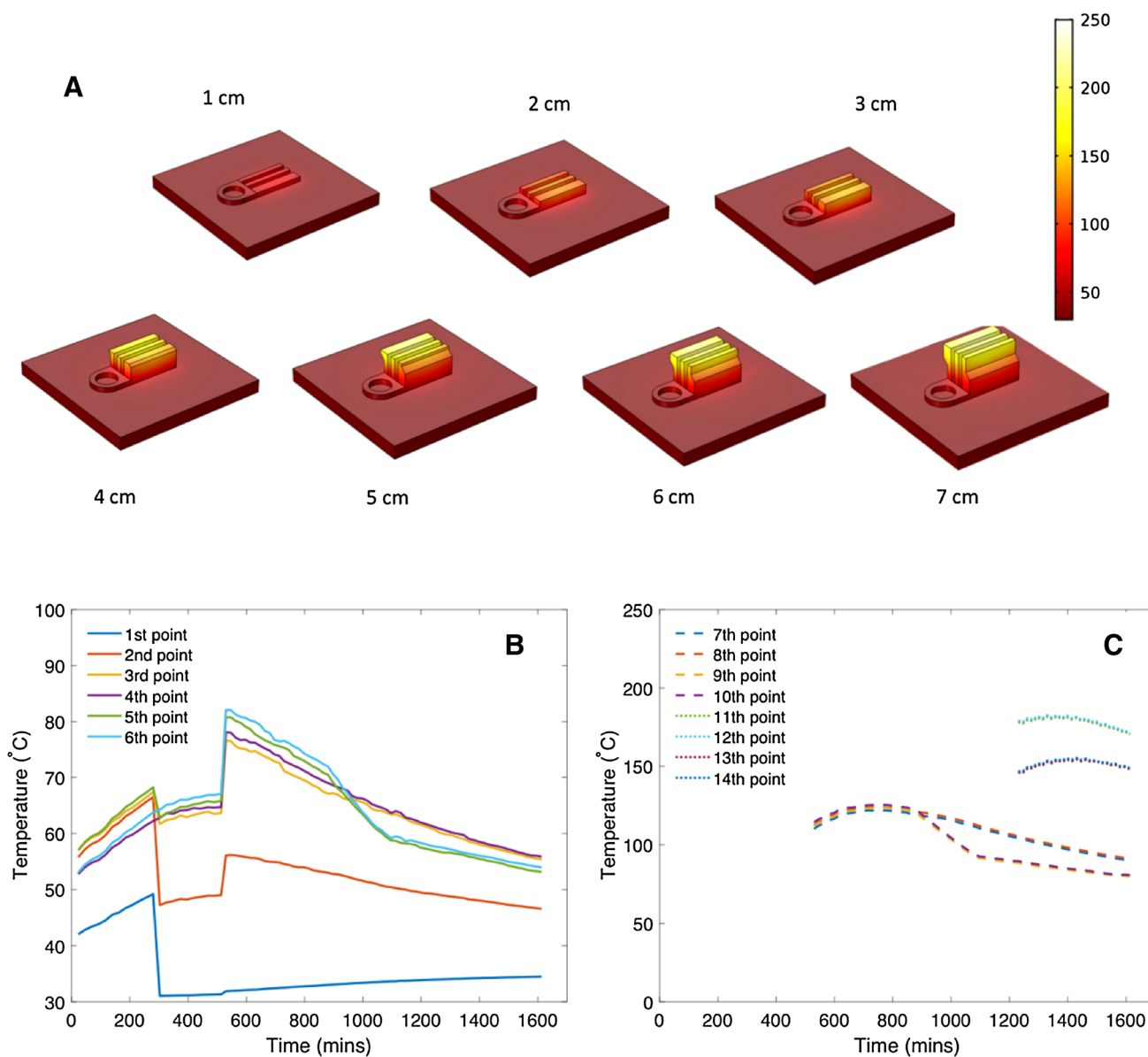


Fig. 9 a Three-dimensional temperature contour maps showing the thermal evolution obtained from the numerical model; **b** and **c** temperatures at the points of interest. The temperature is shown just before the next powder layer was deposited

6.1.2 Small-scale thermal development

While the large-scale perspective shows the gradual temperature increase during the build, the temperature profile on a local scale is essential for microstructural prediction. As examples, the calculated transient temperatures of points 7 and 14 are shown in Fig. 11. As predicted temperatures involve details on multiple time scales, these are plotted in two ways in this figure. In one approach, the time was reset to zero with the addition of each new layer, to illustrate how adjacent tracks influenced thermal history. It was found that tracks more than three hatch spacings away from the point of interest had an insignificant effect on the thermal history.

In a second approach, elapsed time continually increased as new layers were deposited. For example, the 1st layer started from 0 s while the 2nd and 3rd layers started from 70 and 140 s, respectively (for 70 s to complete a layer). According to Fig. 11, the thermal histories from points 7 and 14 are mostly indistinguishable even though one is at the bottom (point 7) and the other near the top of the part (point 14). These thermal histories are similar because: (1) processing parameters and the scanning pattern were consistent for the entire build and (2) the increase in average temperature at point 14 was only around 120 °C above room temperature (see Table 2). From this finding, unless the resting time between layers is very short, or a product contains small features, the

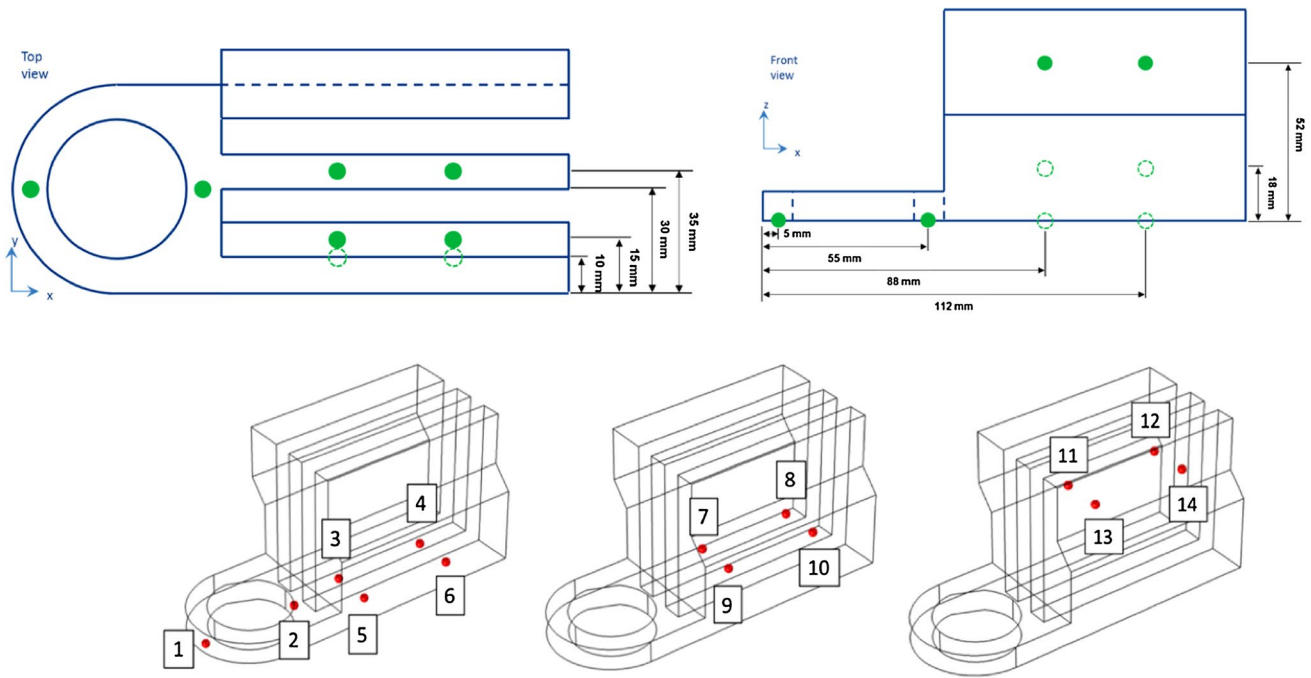


Fig. 10 Points of interest with numbered labels

local temperature history at all points in the product is likely similar. Figure 12a compares the measured temperature and predicted temperature at point 7 while Fig. 12b compares the estimated peak temperature with mean and standard deviations obtained from three thermocouples. The reason for the timing mismatch for the occurrence of the peak temperature in Fig. 12a is that the actual time spent on building the first ten layers varied between 67 and 78 s per layer, whereas the computational approach assumed a constant time interval of 70 s. In addition, even though the peak temperature in the numerical simulation shows a gradual decrease, because of the variation of the time interval between layers, the peak temperature from the experiment fluctuated slightly as seen from the increase in the peak temperature at approximately 350 and 650 s owing to the short time interval between layers.

Additionally, as shown in Fig. 12b, a distinct difference is observed between the predicted and measured thermal

profiles, especially for the first few layers. The reason is because extrapolation of the measured data was needed for the early layers when temperature exceeded the melting point of the material. The extrapolation was necessitated because of the loss of several thermocouples during deposition of these layers. Limited data during complete melting was obtained with a few thermocouples, but a complete thermal cycle for the first and second layers was not achieved for any one thermocouple. Therefore, extrapolation of available thermocouple measurements was used to bound the measured data. Based on the extrapolated data for peak temperatures shown in Fig. 12b, and assuming that melting at 1277 °C was achieved during the first two layers and may also have resulted in superheating of the pool, the model may have over-predicted temperatures by approximately 200 °C. Obviously, this is speculative since measurements of pool temperatures under these conditions are extremely difficult, but based on prior measurements for the powder bed fusion process [25], it is realistic to believe that peak temperatures within the melt pool were no greater than approximately 1500 °C, which would have resulted in over prediction of temperatures by approximately 100 °C.

Nevertheless, according to the comparison with the temperature measurement, the thermal simulation has shown a reasonably accurate prediction, which provides great confidence in the numerical model.

Table 2 Predicted layer temperature increase (in kelvin) from room temperature when the point of interest is built

Point	ΔT_R	Point	ΔT_R	Point	ΔT_R
1	12	6	23	11	148
2	26	7	80	12	149
3	27	8	83	13	116
4	23	9	82	14	117
5	27	10	84		

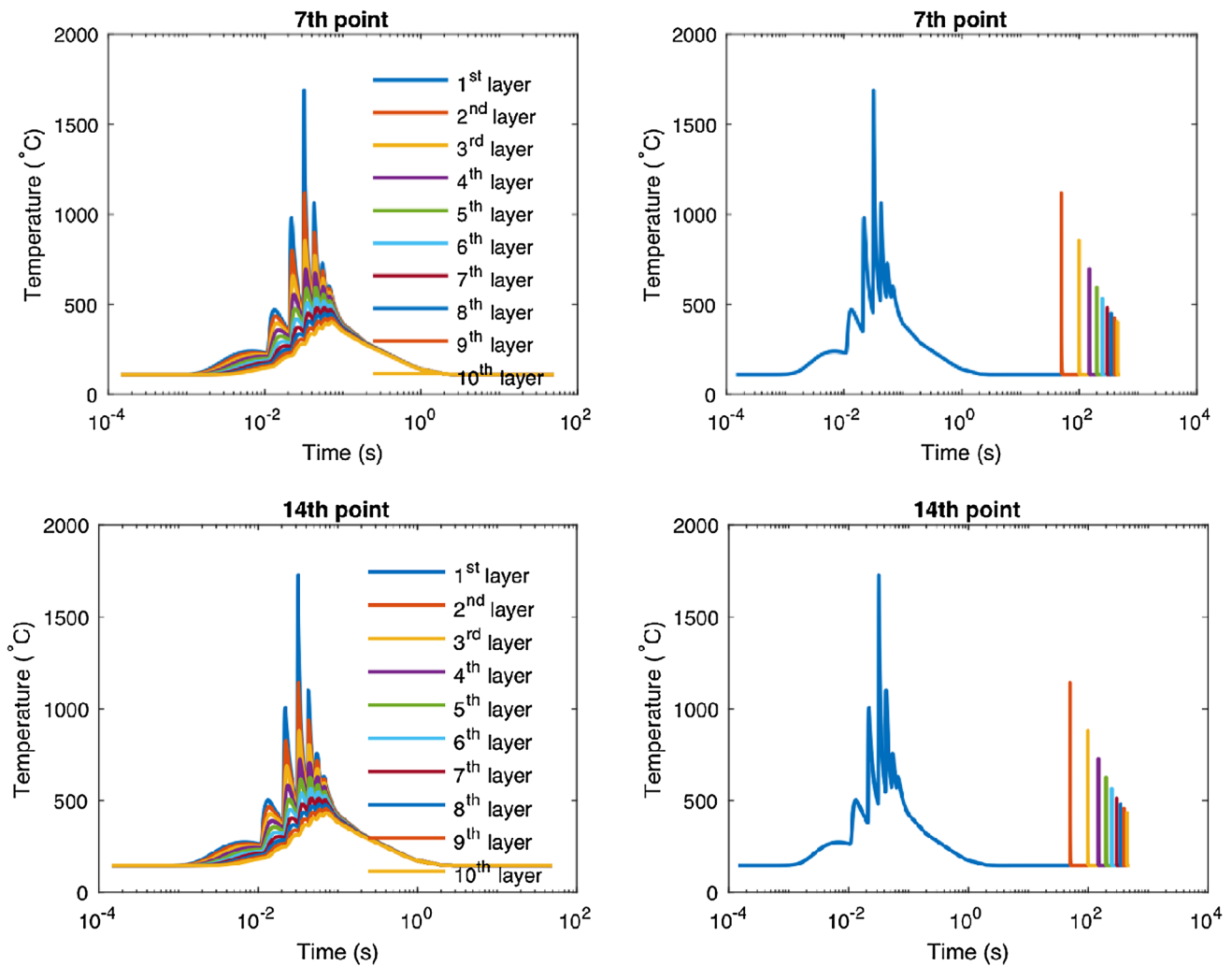


Fig. 11 Numerical prediction of the thermal history at point 7 and 14: left, Time reset to zero at every new layer and right, time continuously increasing

6.2 Melt pool size comparison

Figure 13a shows melt pools on a polished cross-section. The melt pool width and depth at points 7 and 8 (refer to Fig. 10) were measured, taking 20 width and depth measurements in the vicinity of each point of interest. Figure 13b, c compare the measurements and calculations, showing that the melt pool width was slightly over-predicted and the melt pool depth slightly under-predicted. Two possible reasons for the differences are onset of keyholing and measurement difficulties. For process conditions close to the onset of keyholing, the melt pool is deeper and narrower than expected [35]. Second, overlapping from adjacent and overlying tracks can lead to measurement uncertainty.

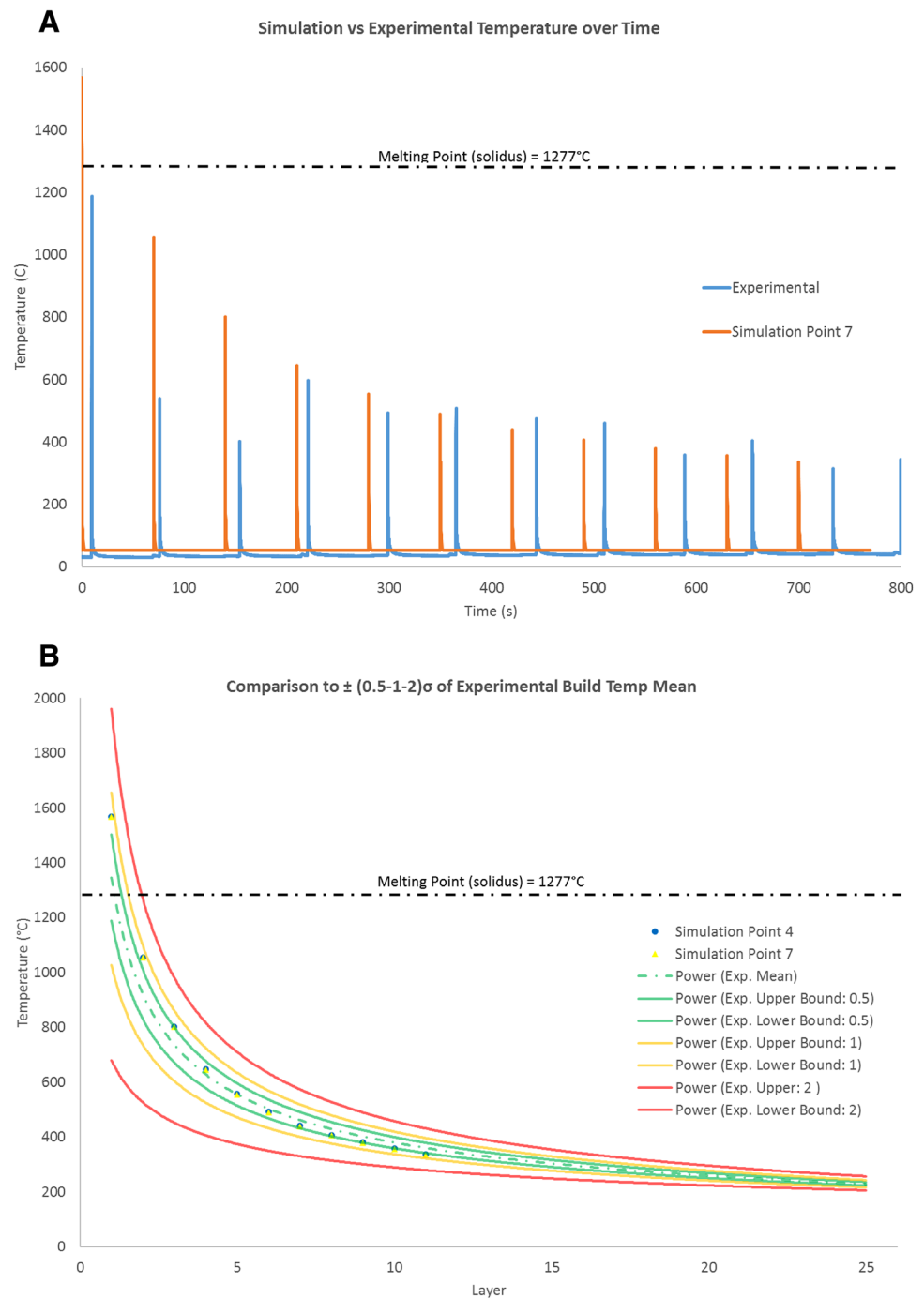
6.3 Microstructural predictions: precipitates, columnar grains and primary dendrite arm spacing (PDAS)

The thermal history was used to predict the following aspects of the microstructure: (1) precipitate formation (using a CCT diagram), (2) columnar or equiaxed grains (using a solidification map), and (3) cell spacing (using the KF equation).

6.3.1 Precipitate formation

The main phase in as-solidified Inconel 718 is expected to be γ (FCC) with possible precipitates (γ' and γ'') although carbides and delta (δ) phase are also possible. A published

Fig. 12 a Transient temperature history comparison between numerical results and measurement and **b** peak temperature history comparison between numerical results and measurement including data uncertainty



CCT diagram for Inconel 718 [13] coupled with the predicted thermal cycle history was used to predict precipitation. The thermal cycle (for deposition of up to 10 layers) at four points of interest (8, 10, 12 and 14) was considered, taking zero time when the temperature first decreased to 1000 °C after solidification (precipitation becomes possible below 1000 °C [36]). The thermal histories of selected points are shown in Fig. 14a, b. The thermal effects of three tracks on either side of the point of interest are included. Only a single temperature peak was observed for subsequent

layers. No precipitation is expected below 600 °C. The temperature history of the four points is similar for temperatures higher than 600 °C, and the thermal history of point 14 only is plotted on the CCT diagram, Fig. 14c. After four more layers had been built, reheating from subsequent layers had only a slight effect on the temperature at a given point of interest. From the CCT diagram, it is clear that precipitation of γ' and γ'' was not likely to happen under these processing parameters because of the tendency of the part to cool rapidly. This conclusion is not definitive, for the following

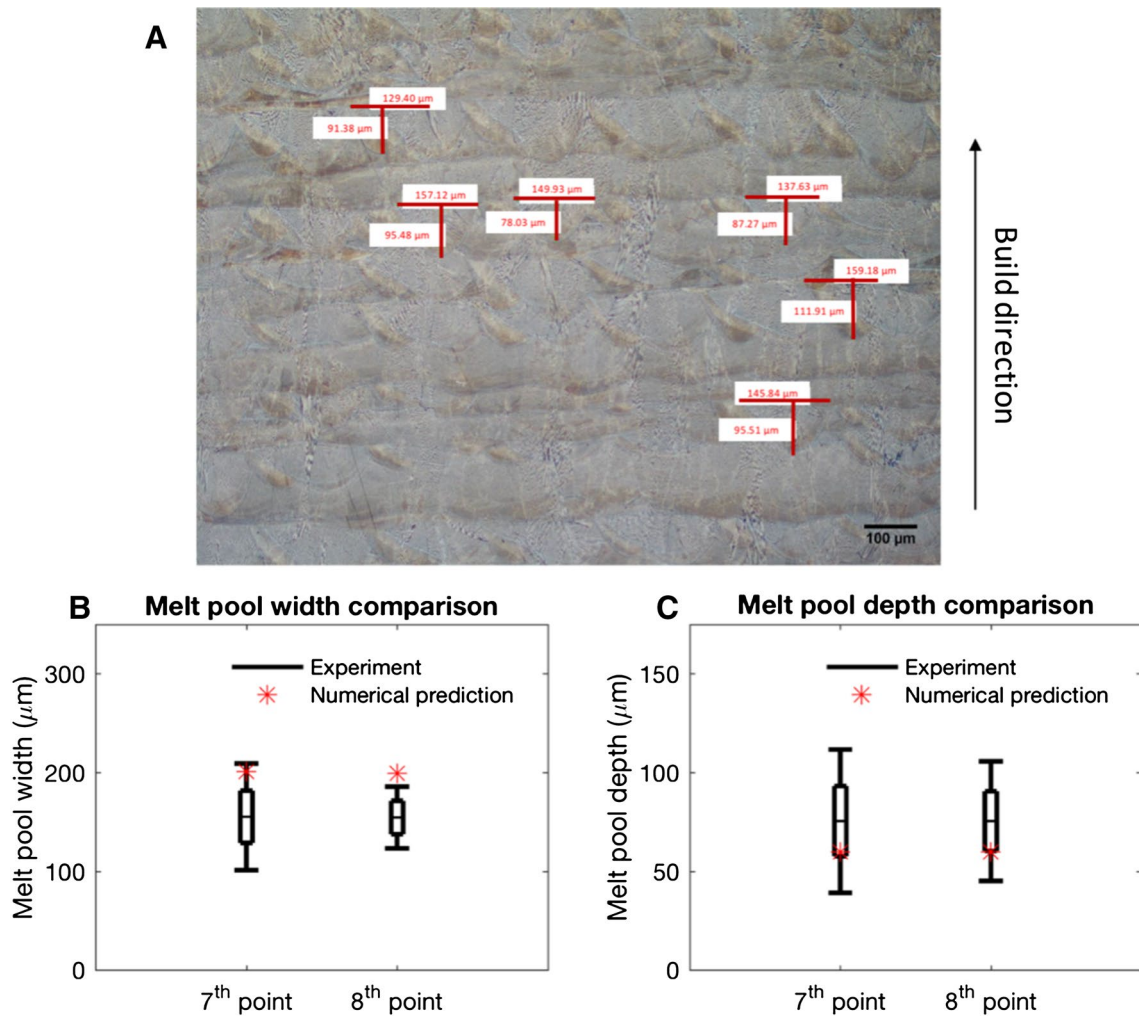


Fig. 13 a Optical micrograph showing melt pools, b Melt pool width comparison at points 7 and 8, c Melt pool depth comparison at point 7 and 8

reasons: first, the CCT diagram is calculated for continuous cooling, and does not apply to repeated cycles of reheating and cooling. Second, microsegregation is likely to change the local composition and so change transformation behavior; microsegregation was not considered in calculation of the CCT diagram.

6.3.2 Solidification map

Various studies, for example, Wei et al. [37], used a Hunt-style solidification map to predict whether the temperature gradient (G) and the solidification rate (R) during solidification would lead to columnar or equiaxed solidification. Figure 15a, b show calculated values of G and R at distances 5, 25, 45, and 65 μm from the top surface of the melt pool. A lower thermal gradient but higher solidification rate is observed near the top surface, with the opposite

close to the bottom of the melt pool. Most data points fall in the columnar grain region, except regions close to the top surface, which are within the mixed grain region. A similar difference in grain types between different locations in the melt pool has been reported in previous studies [22, 38]. The upper region of the melt pool would be remelted upon deposition of the next layer (since the melt-pool depth is significantly larger than the layer thickness), removing the region with predicted mixed grain type. Figure 15c, d show the microstructure of the as-deposited Inconel 718 sample, confirming the columnar grain type. A major cause of uncertainty in this prediction is that the solidification map was calculated for conditions relevant to conventional castings [39], with concentrations of grain nuclei which appear to be too low to be realistic for AM conditions.

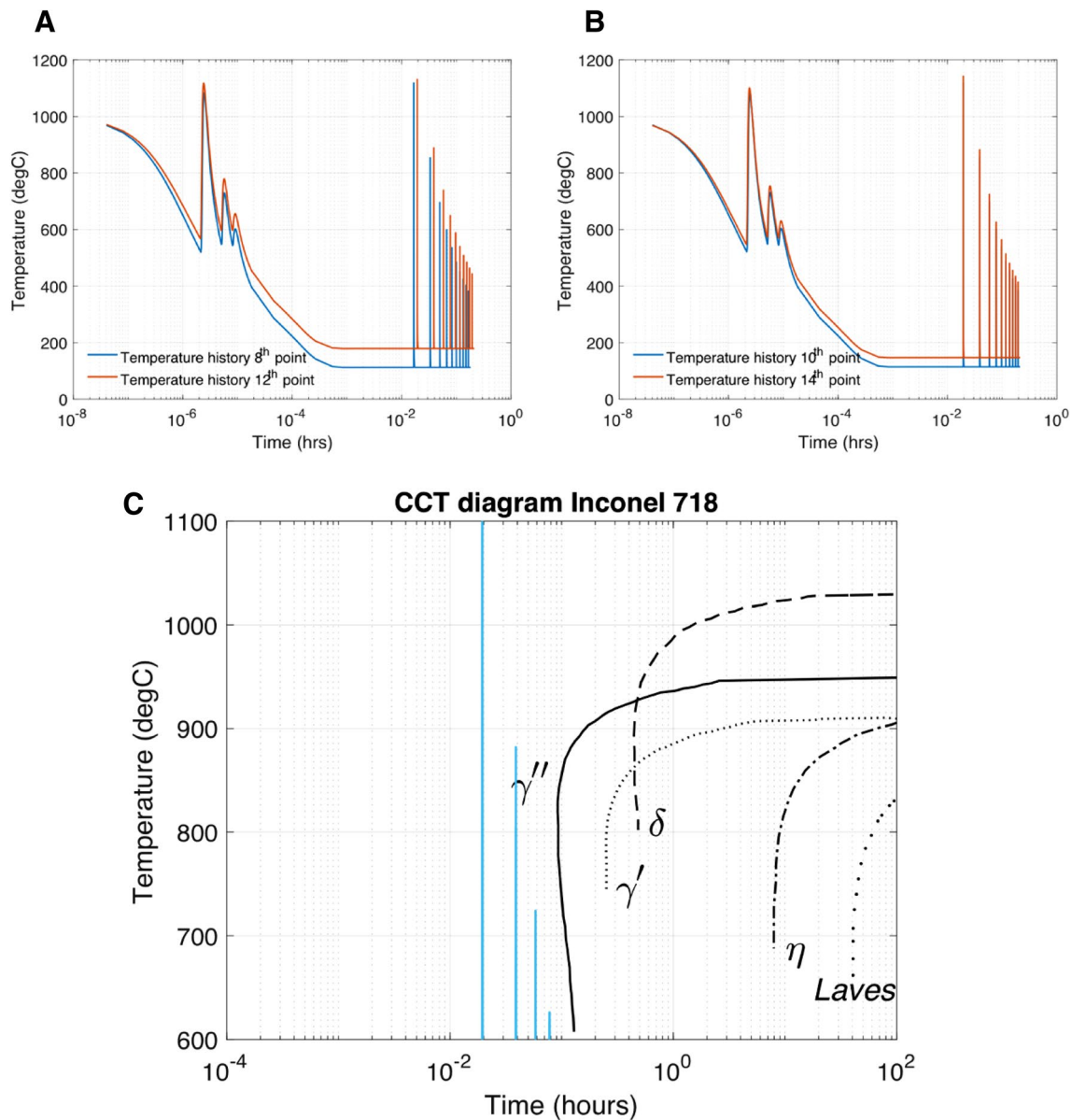


Fig. 14 **a** adjusted thermal history consisting of 10 layers for points 8 and 12, **b** adjusted thermal history consisting of 10 layers for points 10 and 14, and **c** thermal history of point 14 plotted on a CCT diagram for Inconel 718 from ref. [13]

6.3.3 Primary dendrite arm spacing (PDAS)

The primary dendritic arm spacing (λ), or cell spacing, was estimated using Eq. 5 from Kurz and Fisher (KF) [23], and the material properties summarized in Table 3. The partition coefficient is similar to the value used by Nastac et al. [39] to calculate microstructures in conventionally cast IN718, and represents a weighted average for all the elements in the alloy [39].

$$\lambda = 4.3 \left(\frac{\Delta T_0 D \Gamma}{k_0} \right)^{0.25} G^{-0.5} R^{-0.25} \quad (5)$$

The KF model shows that the primary dendrite arm spacing depends on the thermal gradient (G) and the solidification rate (R), which vary within the melt pool [40]. The expected dendrite spacing was evaluated at different positions in the melt pool (30, 40, 50, 60, and 70 μm from the melt-pool surface), spanning the range of locations that were not remelted by subsequent layers (see Fig. 16). Conditions at points 8, 10, 12, and 14 were considered; see Fig. 17a–c. In all cases, the predicted dendrite spacing is approximately 1 μm and increases slightly with increased layer temperature: the PDAS at points 12 and 14 is just larger than at points 8 and 10. This observation agrees well with the experimental

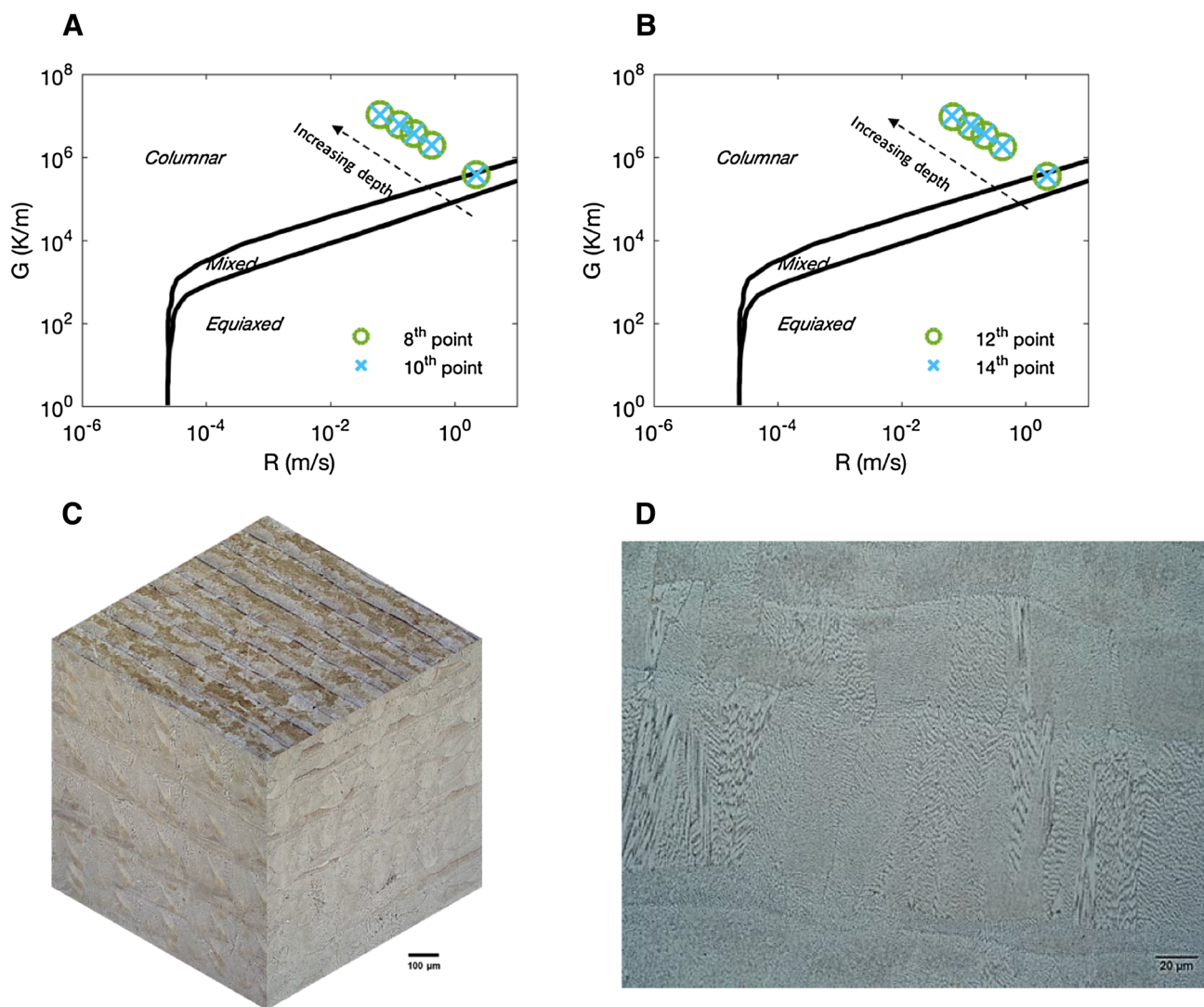


Fig. 15 Temperature gradient (G) and solidification rate (R) at various depths in the melt pool for **a** points 8 and 10 and **b** points 12 and 14. **c** and **d** show optical micrographs at lower and higher magnification, in the vicinity of point 7

Table 3 Inconel 718 physical properties used for KF model [22]

Properties	Value
Solidification interval, ΔT_0	31.9 K
Liquid diffusivity, D	$3 \times 10^{-9} \text{ m}^2/\text{s}$
Partition coefficient, k_0	0.7
Gibbs–Thomson coefficient, Γ	$1.8 \times 10^{-7} \text{ m K}$

study by Ma et al. [41]. The observed PDAS at point 7 and 8 is illustrated in Fig. 18. Measurements of PDAS were obtained from random lines overlaid onto micrographs, which are shown in Fig. 18 as red lines. Twelve measurements were made at each point, with results given in Fig. 19. The mean PDAS at the two points is indistinguishable, and agrees well with the predictions.

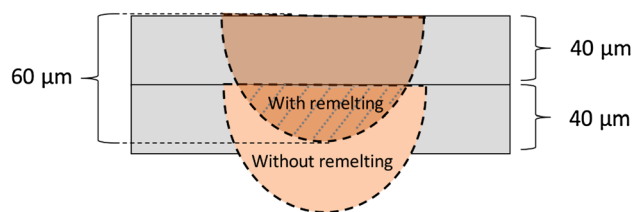


Fig. 16 Illustration of melt pools in two layers, where regions with and without remelting are identified

7 Conclusion

The present study examined the thermal and microstructural evolution in an Inconel 718 product made by

Fig. 17 Calculated temperature gradient (a), solidification rate (b) and PDAS (c) at various depths within the melt pool for points 8, 10, 12, and 14

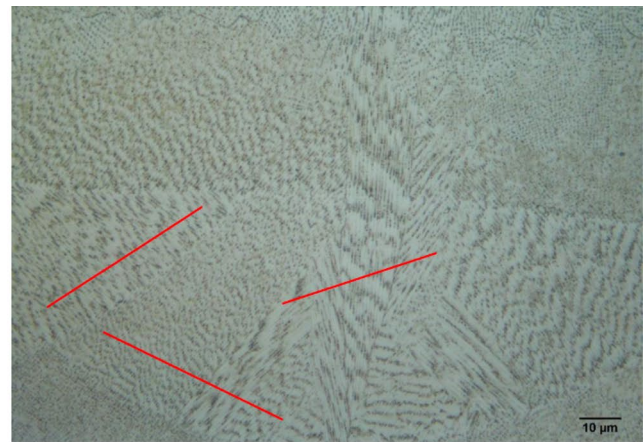
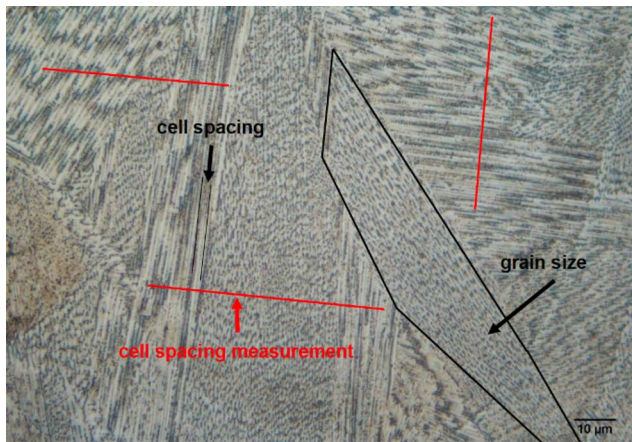
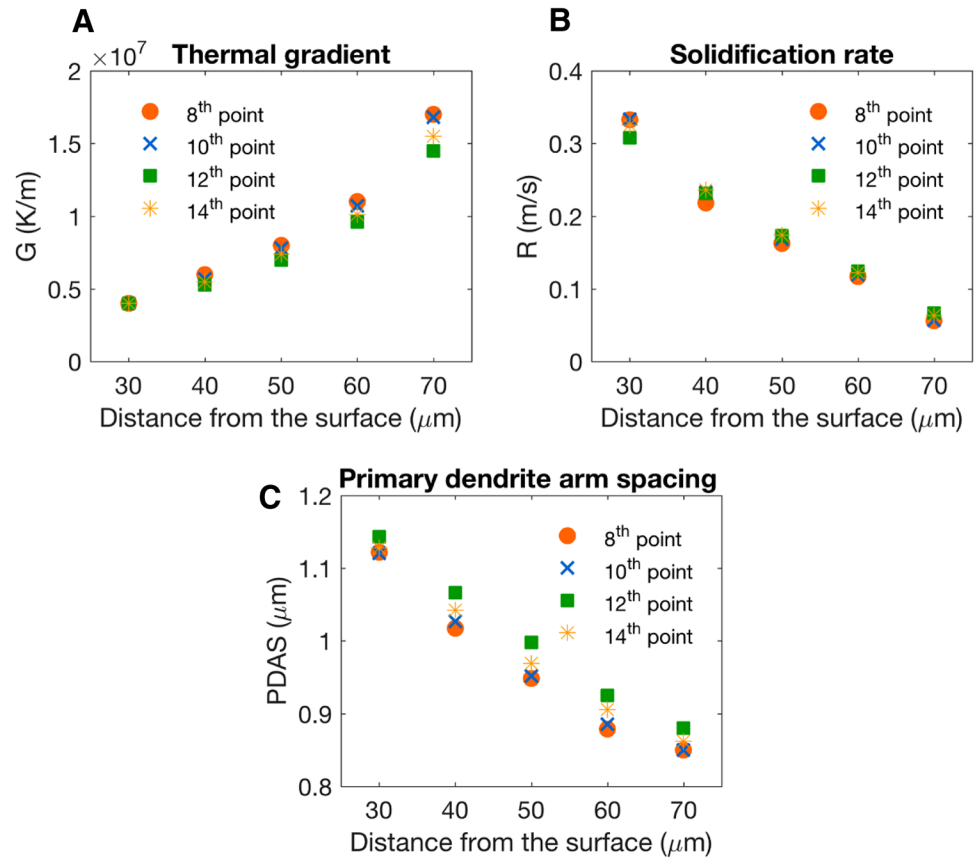


Fig. 18 PDAS measurements at points 7 and 8

laser powder-bed fusion. The product was 7 cm high and required more than 1700 layers to complete the production. The experimental build (including microstructural and thermal measurements) and full numerical analysis were performed independently, considering the thermal history, melt pool size, precipitation, grain type prediction, and primary dendrite arm spacing (PDAS). The numerical simulation was found to be in good agreement with the

actual behavior of the entire product, which constitutes a validation of model. Conclusions from the present study are as follows.

1. The temperature history prediction is validated by the thermal measurement. Calculations predicted only the minor heating of the layers at higher heights with a maximum temperature rise of 250 °C.

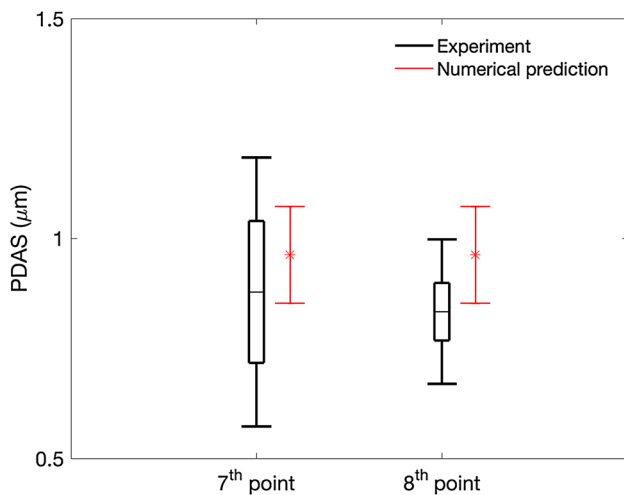


Fig. 19 Comparison of measured and calculated dendrite spacing, showing slight over-prediction

- The thermal model implies that unless a product involves a very short fabrication time or small geometric features, the local transient thermal history of the entire product does not vary, i.e., is the same everywhere except for variations caused by heat build-up.
- The melt pool size was determined by metallography. The numerical predictions tended to over-predict the melt pool width and under-predict the melt pool depth.
- Because of rapid cooling after solidification, age-hardening precipitates (γ' and γ'') are not expected to form. It was noted that recent work has suggested that micro-segregation leads to different precipitation behavior from that suggested by standard TTT or CCT diagrams [14].
- Based on a solidification map, columnar grains are expected for the entire product, in agreement with experimental results.
- The measured primary dendrite arm spacing (PDAS) (cell size) is approximately $1\ \mu\text{m}$, in agreement with the calculations.
- The present study successfully used the computational approach to provide the comprehensive qualification to the powder-bed fusion AM process. A future study can improve by exploring more complex geometries or using the numerical model to engineer desired material characteristics at selected locations.

Acknowledgements PP is grateful for support from the Royal Thai Government and the Bertucci Graduate Fellowship for this research. PCP and ADR acknowledge support from an Early Stage Innovations Grant, number NNX 17AD03G, from NASA's Space Technology Research Grants Program.

Compliance with ethical standards

Conflict of interest On behalf of all authors, the corresponding author states that there is no conflict of interest.

References

- Gao W et al (2015) The status, challenges, and future of additive manufacturing in engineering. *Comput Aided Des* 69:65–89
- Mingareev I, Richardson M (2017) Laser additive manufacturing: going mainstream. *Opt Photon News* 28(2):24–31
- Jia Q, Gu D (2014) Selective laser melting additive manufactured Inconel 718 superalloy parts: high-temperature oxidation property and its mechanisms. *Opt Laser Technol* 62:161–171
- Wang X, Keya T, Chou K (2016) Build height effect on the Inconel 718 parts fabricated by selective laser melting. *Procedia Manuf* 5:1006–1017
- Yan W et al (2017) Multi-physics modeling of single/multiple-track defect mechanisms in electron beam selective melting. *Acta Mater* 134:324–333
- Xia M et al (2016) Influence of hatch spacing on heat and mass transfer, thermodynamics and laser processability during additive manufacturing of Inconel 718 alloy. *Int J Mach Tools Manuf* 109:147–157
- Romano J, Ladani L, Sadowski M (2016) Laser additive melting and solidification of Inconel 718: finite element simulation and experiment. *Jom* 68(3):967–977
- Promopattum P, Onler R, Yao S-C (2017) Numerical and experimental investigations of micro and macro characteristics of direct metal laser sintered Ti-6Al-4V products. *J Mater Process Technol* 240:262–273
- Denlinger ER et al (2017) Thermomechanical model development and in situ experimental validation of the laser powder-bed fusion process. *Addit Manuf* 16:73–80
- Masoomi M, Thompson SM, Shamsaei N (2017) Laser powder bed fusion of Ti-6Al-4V parts: thermal modeling and mechanical implications. *Int J Mach Tools Manuf* 118:73–90
- Zhao X, Promopattum P, Yao SC (2015) Numerical modeling of non-linear thermal stress in direct metal laser sintering process of titanium alloy products. In: *Proceedings of the 1st thermal and fluid engineering summer conference*, August 2015, New York
- Peyre P et al (2008) Analytical and numerical modelling of the direct metal deposition laser process. *J Phys D Appl Phys* 41(2):025403
- Sames WJ et al (2014) Thermal effects on microstructural heterogeneity of Inconel 718 materials fabricated by electron beam melting. *J Mater Res* 29(17):1920–1930
- Lass EA et al (2017) Formation of the Ni₃Nb δ -phase in stress-relieved Inconel 625 produced via laser powder-bed fusion additive manufacturing. *Metall Mater Trans A* 48:5547–5558
- Tian Y et al (2014) Rationalization of microstructure heterogeneity in Inconel 718 builds made by the direct laser additive manufacturing process. *Metall Mater Trans A* 45(10):4470–4483
- Lu Y et al (2015) Study on the microstructure, mechanical property and residual stress of SLM Inconel-718 alloy manufactured by differing island scanning strategy. *Opt Laser Technol* 75:197–206
- Liu J, To AC (2017) Quantitative texture prediction of epitaxial columnar grains in additive manufacturing using selective laser melting. *Addit Manuf* 16:58–64
- Hunt J (1984) Steady state columnar and equiaxed growth of dendrites and eutectic. *Mater Sci Eng* 65(1):75–83

19. Ghosh S, Ma L, Ofori-Opoku N, Guyer JE (2017) On the primary spacing and microsegregation of cellular dendrites in laser deposited Ni–Nb alloys. *Modell Simul Mater Sci Eng* 25(6)
20. Kurz W, Fisher D (1981) Dendrite growth at the limit of stability: tip radius and spacing. *Acta Metall* 29(1):11–20
21. Hunt J (1979) Cellular and primary dendrite spacings. In: *Solidification and casting of metals*\Proc. Conf\, Sheffield, England
22. Liang Y-J et al (2016) Prediction of primary dendritic arm spacing during laser rapid directional solidification of single-crystal nickel-base superalloys. *J Alloy Compd* 688:133–142
23. Kurz W, Fisher DJ (1998) *Fundamentals of solidification*. Tans Tech Publications Ltd., Aedermannsdorf
24. Martukanitz R et al (2014) Toward an integrated computational system for describing the additive manufacturing process for metallic materials. *Addit Manuf* 1:52–63
25. Lia F, Park JZ, Keist JS, Joshi S, Martukanitz RP (2018) Thermal and microstructural analysis of laser-based directed energy deposition for Ti-6Al-4V and Inconel 625 deposits. *Mater Sci Eng A* (Submitted)
26. Bonacina C et al (1973) Numerical solution of phase-change problems. *Int J Heat Mass Transf* 16(10):1825–1832
27. Hosaeus H et al (2001) Thermophysical properties of solid and liquid Inconel 718 alloy. *High Temp High Press* 33(4):405–410
28. Sainte-Catherine C et al. (1991) Study of dynamic absorptivity at 10.6 μm (co2) and 1.06 μm (nd-yag) wavelengths as a function of temperature. *Le Journal de Physique IV* 1(C7):C7-151–C7-157
29. Montgomery C, Beuth J, Sheridan L, Klingbeil N (2015) Process mapping of Inconel 625 in laser powder bed additive manufacturing. In: *Solid Freeform Fabrication Symposium*, pp 1195–1204
30. Lee Y, Zhang W (2016) Modeling of heat transfer, fluid flow and solidification microstructure of nickel-base superalloy fabricated by laser powder bed fusion. *Addit Manuf* 12:178–188
31. Chiumenti M et al (2017) Numerical modelling and experimental validation in selective laser melting. *Addit Manuf* 18:171–185
32. Sadowski M et al (2016) Optimizing quality of additively manufactured Inconel 718 using powder bed laser melting process. *Addit Manuf* 11:60–70
33. Lia F et al (2017) Partitioning of laser energy during directed energy deposition. *Addit Manuf* 18:31–39
34. Tang M, Pistorius PC, Beuth JL (2017) Prediction of lack-of-fusion porosity for powder bed fusion. *Addit Manuf* 14:39–49
35. Trapp J et al (2017) In situ absorptivity measurements of metallic powders during laser powder-bed fusion additive manufacturing. *Appl Mater Today* 9:341–349
36. Radavich JF (1989) The physical metallurgy of cast and wrought alloy 718. In: *Conference proceedings on superalloy*, vol. 718, pp 229–240
37. Wei H, Mukherjee T, DebRoy T (2016) Grain growth modeling for additive manufacturing of nickel based superalloys. In: Holm EA et al (eds) *Proceedings of the 6th international conference on recrystallization and grain growth (ReX&GG 2016)*. Springer, Cham
38. Wang G, Liang J, Zhou Y, Jin T, Sun X, Hu Z (2017) Prediction of dendrite orientation and stray grain distribution in laser surface-melted single crystal superalloy. *J Mater Sci Technol* 33(5):499–506
39. Nastac L, Valencia JJ, Tims ML, Dax FR (2001) Advances in the solidification of IN718 and RS5 alloys. In: *Proceedings of superalloys 718, 625, 706 and various derivatives*
40. Bontha S et al (2009) Effects of process variables and size-scale on solidification microstructure in beam-based fabrication of bulky 3D structures. *Mater Sci Eng A* 513:311–318
41. Ma M, Wang Z, Zeng X (2015) Effect of energy input on microstructural evolution of direct laser fabricated IN718 alloy. *Mater Charact* 106:420–427